Available online at www.sciencedirect.com

ScienceDirect

International Journal of Solids and Structures 45 (2008) 2470–2492

INTERNATIONAL JOURNAL OF SOLIDS AND STRUCTURES

www.elsevier.com/locate/ijsolstr

Deformations of a clamped–clamped elastica inside a circular channel with clearance

Zhi-Hao Lu, Jen-San Chen *

Department of Mechanical Engineering, National Taiwan University, Taipei 10617, Taiwan

Received 28 July 2007; received in revised form 5 December 2007
Available online 15 December 2007

Abstract

In this paper, we study the planar deformations of an elastica inside a circular channel with clearance. One end of the elastica is fully clamped, while the other end is partially clamped in the lateral direction and is subject to a pushing force longitudinally. In the experiment we first observe various deformation patterns after pushing the elastica through the partial clamp. Both symmetric and asymmetric deformations are recorded. Special attention is focused on the contact conditions between the elastica and the circular channel. In order to analyze the elastica deformation theoretically, we first divide the elastica into several elementary sub-domains depending on the contact condition between the elastica and the circular channel. In each sub-domain the elastica is either loaded only at the ends or in full contact with the outer wall. Armed with these basic equilibrium analyses, we proceed to calculate and classify the loaded elastica into several deformation patterns. Finally, we present the load-deflection curves, both theoretically and experimentally, which relate the longitudinal forces at both ends to the elastica length increase inside the channel. The branching phenomena predicted theoretically agree fairly well quantitatively with the experimental measurements.

Keywords: Constrained elastica; Circular channel; Deformation patterns

---

1. Introduction

The primary goal of the study on constrained elastica is to understand the behavior of a thin rod or plate under external compression when it is subject to lateral boundary constraint with clearance. This type of analysis can be considered as an extension of the classical elastica theory initiated by Euler and Lagrange over two centuries ago (Love, 1944; Timoshenko and Gere, 1961). For instance, Domokos et al. (1997) and Holmes et al. (1999) investigated the planar buckling patterns of an elastic hinged–hinged bar constrained inside a straight channel with clearance. Their works were motivated by a need to understand the buckling behavior of polypropylene fibers in a 'stuffer box' manufacturing environment for non-woven fabrics. Plaut et al. (1999, 2004) studied the deflections and buckling of a bent elastica in contact with a flat surface. Their works found

---

[*] Corresponding author. Tel.: +886 2 33662693; fax: +886 2 23631755.
E-mail addresses: jschen@ntu.edu.tw, jschen@ccms.ntu.edu.tw (J.-S. Chen).

0020-7683/$ - see front matter © 2007 Elsevier Ltd. All rights reserved.
doi:10.1016/j.ijsolstr.2007.12.004

application in electronic circuit strip wiring in lap-top computers. Chai (2002, 2006) carried out a combined experimental/analytical work to elucidate the energy absorption potential of laterally confined bars under monotonically increasing edge displacement. Roman and Pocheau (2002) used an elastica model to investigate the post-buckling response of bilaterally constrained thin plates subject to a height reduction. The uniqueness of solutions for constrained elastica was addressed by Pocheau and Roman (2004).

In the drilling industry, engineers are interested in the buckling of a tube in an inclined wellbore under the action of its own weight and a compressive force at its upper end. The deformation of the constrained tube may be planar (Paslay and Bogy, 1964) or helical (Huang and Pattillo, 2000). In the case when the wellbore is curved, Wu and Juvkam-Wold (1995) studied the buckling and lockup of the tubes under compressive end force. Kuru et al. (2000) experimentally studied the buckling behavior of pipes and its influence on the axial force transfer in directional wells. The recent development in the research on the buckling of tubes inside wellbores can be found in a review paper by Cunha (2004). Recently, Chen and Li (2007) studied the deformation of a planar elastica under follower end loads inside a circular channel with clearance. Their work was motivated by the mechanics problem observed in the stent deployment procedure.

In this paper, we extend the analysis in Chen and Li (2007) by studying the deformation patterns of a planar elastica under a conservative pushing force within a circular channel. At one end of the circular channel the elastica is fully clamped. At the other end the lateral displacement and slope of the elastica are fixed, while the elastica is allowed to slide in and out of the clamp in the longitudinal direction.

2. Problem description

Fig. 1 shows a circular channel with outer and inner radii r_o and r_i. ψ is the span angle of the circular channel. An elastic strip, or the planar elastica, is placed inside the channel. One end of the elastica is fully clamped at the left end B of the channel. On the right end A the elastica is partially clamped. By partially clamped we mean that the strip is allowed to slide freely through the clamp, while the lateral displacement and slope at A are fixed. The strip will be under external pushing force at end A. As a result of this pushing force, the strip originally outside the channel will slide through the partial clamp, and the shape of the strip inside the channel will change accordingly.

It is noted that in Fig. 1 we only show the elastica inside the channel. We assume that the elastic strip is inextensible and is stress-free when it is straight. The strip is uniform in all mechanical properties along its length. It is assumed that the thickness of the elastic strip is much smaller than the clearance $r_o - r_i$ of the channel. Before the application of the external pushing force, the elastica is in the form of a circular shape with constant bending moment throughout the entire length, as shown by the circular dashed curve in Fig. 1. The original length of the elastica inside the circular channel is denoted as l_o. The solid curve in Fig. 1 represents the first stage of the elastica deformation when an external force F_A is applied to push in the elastica at end A. The total length of the strip inside the channel is increased by Δl. In Fig. 1 the elastica

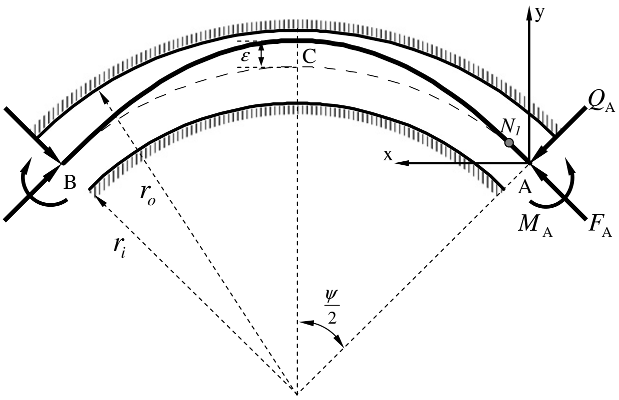

Fig. 1. Deformation pattern 1. Elevated middle point.

is not in contact with the circular walls yet. It is not hard to envision that when the pushing force increases, the elastica will contact the outer radius of the channel first. However, it is not obvious how the elastica will behave thereafter. The purpose of this paper is to study the behavior of the elastica in response to the external pushing force.

3. Qualitative experimental observations

The easiest way to visualize the elastica deformation is to build an experimental apparatus as described in Section 2 and make observations. The schematic diagram of the experimental set-up is shown in Fig. 2. We manufactured a circular channel with outer radius $r_o = 40$ cm, inner radius $r_i = 32$ cm, and span angle $\psi = 90°$. The channel is manufactured by a CNC milling machine on a polypropylene block. The elastica is made of carbon steel strip (type SK5) with Young's modulus 205 GPa and mass density 7830 kg/m^3. The cross section of the elastica is 46 mm × 0.1 mm. On the right end of the channel the strip can be pushed in by hand through the small clearance of a pair of flat blocks, which serves as the partial clamp as described in the last section. The left end of the elastica is fully clamped in an aluminum block. We design a guide rail on the bottom of the left clamp, which is attached to a laboratory-built load cell as shown in Fig. 2. When observing the elastica deformation qualitatively the left clamp is fixed on the guide rail by screws. When measuring the longitudinal reactive force on the left end, the left clamp is allowed to slide on the rail slightly. It is noted that in the experiment we control the length of the strip being pushed in the channel. Therefore, this is a displacement control procedure instead of a load control procedure.

Figs. 3–5 show the photographs of the elastica deformations we observed in the laboratory after fixing the left clamp on the rail. Fig. 3 shows 12 deformation patterns in one of the experiments. In Fig. 3(1) the elastica is pushed in a length $\Delta l = 2$ cm. The middle point of the elastica is lifted up a small distance. This deformation pattern has been demonstrated in Fig. 1. After the strip is pushed in 4 cm, the elastica makes a point contact with the outer wall, as shown in Fig. 3(2). When Δl increases to 7 cm, the point contact at the middle point evolves to distributed contact in the middle region, as shown in Fig. 3(3).

After fixing the end of the strip on the right and poking the strip in the middle by hand, the elastica deformation jumps to Fig. 3(4). In Fig. 3(4) the middle point of the elastica floats in the air while the neighboring segments remain in contact with the outer wall. We call the middle section a "folding" segment. If we slightly disturb the deformation in Fig. 3(4), the elastica will return to this deformation. In other words, this equilibrium configuration is "isolated." It is not clear by eyesight whether the neighboring segments are in point contact or in distributed contact with the outer wall. However, our analysis later shows that if the equilibrium configuration is isolated these segments must be in point contact with the outer wall.

We next push up the middle point in Fig. 3(4) by hand, and observe that the elastica deformation evolves to Fig. 3(5). There are two major differences between Fig. 3(4) and (5). The first difference is that the middle point

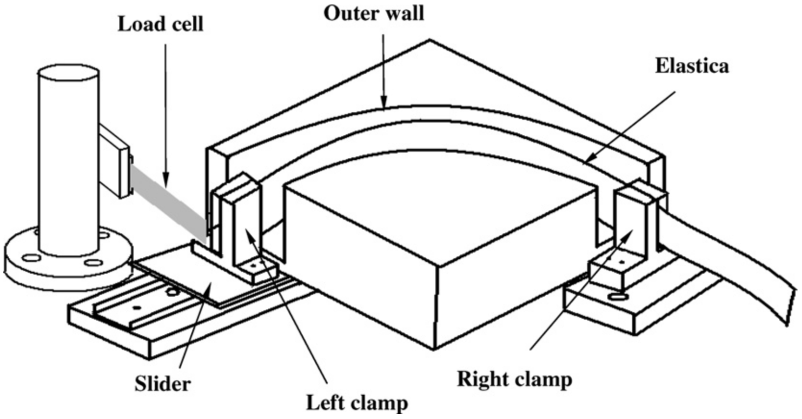

Fig. 2. Schematic diagram of the experimental set-up.

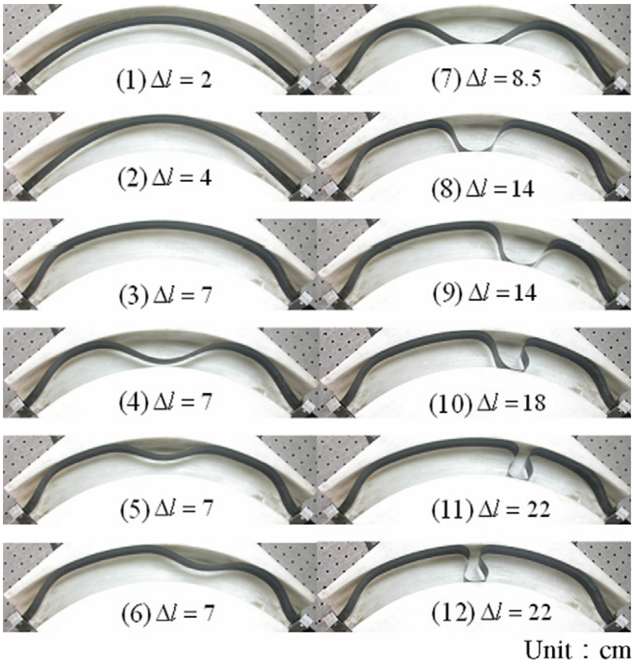

Fig. 3. Experimental observations of elastica deformation with one folding segment.

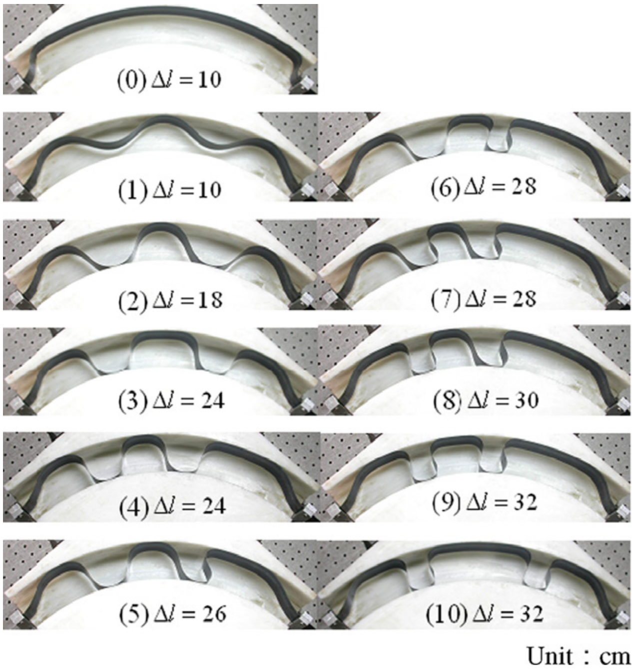

Fig. 4. Experimental observations of elastica deformation with two folding segments.

in Fig. 3(5) is higher and the contact regions in the neighboring segments are longer, which suggests distributed contacts. The second difference is that if we disturb deformation 3(5) slightly, the middle folding segment of the elastica can move aside and the deformation becomes asymmetric, as shown in Fig. 3(6). In other words, multiple equilibrium configurations can coexist for a single Δl. Our analysis later shows that this kind of neu-

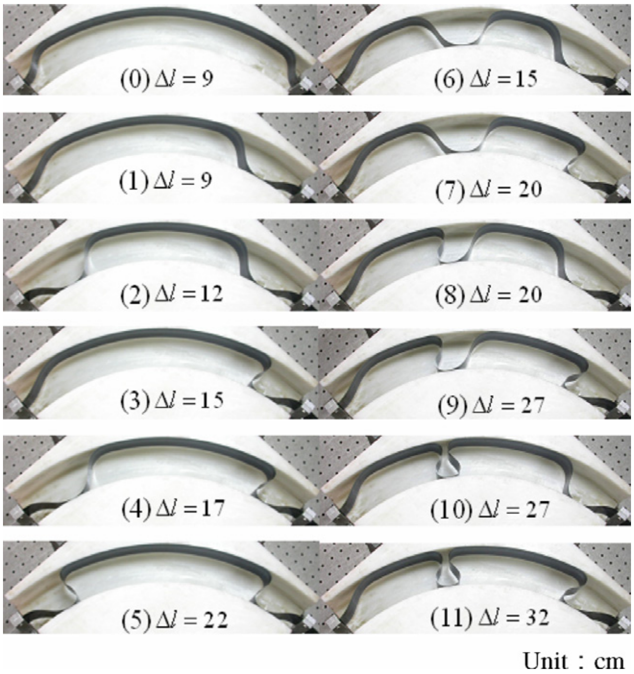

Fig. 5. Experimental observations of elastica deformation with opposite curvatures at both ends.

tral stability characteristics exists only when the neighboring segments are in distributed contact with the outer wall.

If we restart the experiment from Fig. 3(4) and increase Δl to 8.5 cm, the middle point will contact the inner wall while the neighboring segments remain in contact with the outer wall, as shown in Fig. 3(7). Again, slight disturbance will not move the elastica away from this deformation pattern. This feature suggests that the elastica touches the outer wall in point contacts. If we increase Δl to 14 cm, the neighboring segments will become distributed contact with the outer wall, while the middle point remains in point contact with the inner wall, as shown in Fig. 3(8). Similar to the case in Fig. 3(5), the middle folding segment of the elastica can be moved aside by hand and the deformation becomes asymmetric, as shown in Fig. 3(9).

When Δl continues to increase to 18 cm the deformation in Fig. 3(9) evolves to Fig. 3(10), in which the folding segment is "slanted." The original folding segment in Fig. 3(9) is called "regular." When Δl continues to increase to 22 cm, it is possible to produce the deformations in Fig. 3(11) (asymmetric) and (12) (symmetric) by pushing and pulling the strip by hand. The difference between Fig. 3(8) and (12) (also between Fig. 3(9) and (11)) is the shape of the folding segment. The folding segments in Fig. 3(11) and (12) appear to be undergoing a necking process, in which the width near the base on the outer wall becomes smaller. We call this type of folding segment "Ω-shaped." It is noted that the Ω-shaped folding segment can stay in any position between Fig. 3(11) and (12). The reason we list the last five deformations from 3(8) to 3(12) is that the external pushing force required to produce these deformations are theoretically the same. In other words, multiple equilibrium configurations coexist with the same pushing force.

Fig. 4 shows the photographs of the elastica deformation in another experimental procedure. The elastica remains in deformation 4(0) when $\Delta l = 10$ cm. After pulling down the two quarter points of the elastica by hand we can produce the deformation in Fig. 4(1), in which the elastica is in contact with the outer wall at three points. The two middle points of the two folding segments are floating in the air. When Δl increases to 18 cm, the two folding segments touch the inner wall, as shown in Fig. 4(2). As Δl increases to 24 cm, the three point contacts on the outer wall evolve to three distributed contacts, as shown in Fig. 4(3). Again, as long as the contacts on the outer wall become distributed, it is possible to move the distributed contact region by hand to produce asymmetric deformations as shown in Fig. 4(4) while fixing Δl at 24 cm. As Δl increases to 26 cm, the right folding segment in Fig. 4(5) becomes slanted, as shown in Fig. 4(5). If Δl is increased to 28 cm, the deformation could evolve to the shape in Fig. 4(6) and (7). As Δl increases to 30 cm and 32 cm, the deformation evolves to Fig. 4(8) and (9), respectively. The deformations 4(4)–4(9) are all asymmetric. The main difference among them is the combination of different folding segments, i.e., regular–regular (Fig. 4(4)), regular–slanted (Fig. 4(5)), regular-Ω-shaped (Fig. 4(6)), slanted–slanted (Fig. 4(7)), Ω-shaped–slanted (Fig. 4(8)), Ω-shaped–Ω-shaped (Fig. 4(9)). If we move the right folding segment in Fig. 4(9) by hand to the right we can produce a symmetric deformation pattern as shown in Fig. 4(10). It is noted that the pushing forces required to produce the eight deformations from 4(3) to 4(10) are theoretically the same. Moreover, the reactive longitudinal forces on the left clamps are equal to their counterparts on the right.

Fig. 5 shows another experimental procedure starting from deformation in Fig. 5(0) at $\Delta l = 9$ cm. At this Δl the elastica deformation can be changed to Fig. 5(1) by pushing down the right hand side of the strip by hand. This action changes the curvature of the strip near the end on the right, which results in an asymmetric deformation. If we continue to increase Δl to 12 cm and push down the left hand side of the strip by hand, the elastica deformation becomes symmetric again as shown in Fig. 5(2). If we push back the left segment in Fig. 5(2) and return the elastica to the shape in Fig. 5(1) and continue to increase Δl to 15 cm, the deformation evolves to Fig. 5(3). We then push down the left hand side of the elastica in Fig. 5(3) and increase Δl to 17 cm to produce the deformation in Fig. 5(4). The main difference between Fig. 5(1) and (3) (and also between Fig. 5(2) and (4)) is that the folding segment on the right end becomes Ω-shaped. As Δl increases to 22 cm, the elastica deformation becomes symmetric again, as shown in Fig. 5(5). It is noted that the pushing forces on the right required to produce the deformations in Fig. 5(1)–(5) are theoretically the same. However, the reactive longitudinal force on the left clamp can be theoretically different from the external pushing forces on the right. This fact is different from the other asymmetric deformations presented in Figs. 3(9)–(11) and 4(4)–(9).

If we restart the experiment in Fig. 5(3) and push down the middle section of the strip we can produce the deformation as shown in Fig. 5(6), which is asymmetric with two point contacts on the inner wall and two distributed contacts on the outer wall. When Δl increases to 20 cm the elastica deformation evolves to Fig. 5(7), with the folding segment on the right end undergoing a necking process while the left folding segment remaining unchanged. By moving the left folding segment in Fig. 5(7) to the left, the deformation evolves to Fig. 5(8). As Δl increases to 27 cm, the deformation evolves to Fig. 5(9). While fixing Δl at 27 cm, we can produce deformation in Fig. 5(10) by moving the left folding segment to the left by hand. As Δl increases to 32 cm the elastica deformation evolves to Fig. 5(11). Two comments are worth mentioning regarding deformations 5(6)–5(11). First of all, these deformations may be compared in pairs, i.e., Fig. 5(6)–(8) and (9)–(11). The left folding segments of each pair remain unchanged while one of the right folding segments undergoes necking process. Second, the pushing forces required to produce these six deformations are theoretically the same. The reactive longitudinal forces on the left clamp for these six deformations are also theoretically the same. However, these left longitudinal forces are different from the external pushing forces on the right.

Several observations in Figs. 3–5 may be summarized before we leave this section. (1) First of all these photos show some possible deformation patterns produced in the laboratory by controlling the strip length increment inside the channel for a specific geometry, i.e., $r_o = 40$ cm, $r_i = 32$ cm, and $\psi = 90°$. We have no intention to claim that these deformations are complete. It is certainly possible to produce even more complicated deformation patterns involving more than two folding segments with larger Δl. (2) While the boundary conditions at both ends are the same, the deformations can be symmetric with respect to the central radius or completely asymmetric. (3) For the case when the contacts on the outer wall are distributed the folding segments of the elastica can be moved at will within certain range. As a consequence the deformation may become asymmetric. For instance, see Fig. 3(5) and (6). On the other hand, if the elastica is in point contact with the outer wall, the equilibrium configuration appears to be isolated. In other words, the elastica returns to the symmetric deformation following slight disturbance. For instance, see Fig. 3(4). (4) In some cases for fixed Δl, there exist multiple isolated equilibrium positions. In order to change the deformation from one configuration to the other, pushing or pulling the elastic strip inside the channel is required.

4. Equilibrium equations of sub-domains

One of the major interests of this paper is to analyze the elastica deformations as observed in Section 3. Once the elastica is in contact with the circular walls, the analysis of the shape of the elastica must be conducted in a piece-wise manner. In other words, the domain of the elastica is divided into sub-domains. In each sub-domain the elastica is either loaded only at the ends or the whole sub-domain is in full contact with the channel walls. There are six different types of sub-domains which can be observed when a clamped–clamped elastic strip is placed inside a circular channel with clearance. The difference between these six sub-domains lies in their boundary conditions or the contact conditions, as listed in Table 1. Similar sub-domain analysis was first proposed by Domokos et al. (1997) for a hinged–hinged bar constrained in straight walls. In the following we discuss how these boundary conditions or contact conditions affect the equilibrium equations.

4.1. Clamped–clamped sub-domain

Clamped–clamped sub-domain (listed as case (a) in Table 1) occurs only when the whole elastica is a sub-domain, as shown in Fig. 1. The strip is in the form of a circular shape before the external longitudinal force F_{A} is applied. When F_{A} increases from zero, the middle point of the strip will be elevated. The deformation is symmetric with respect to the central radius, as observed experimentally in Fig. 3(1).

First of all we establish an xy-coordinate system with the origin at point A. The moment equation at any point (x, y) of the deformed strip can be written as

$$EI\frac{\mathrm{d}\theta}{\mathrm{d}s} = \left(-Q_{\mathrm{A}}\sin\frac{\psi}{2} - F_{\mathrm{A}}\cos\frac{\psi}{2}\right)y + \left(-Q_{\mathrm{A}}\cos\frac{\psi}{2} + F_{\mathrm{A}}\sin\frac{\psi}{2}\right)x + M_{\mathrm{A}} \tag{1}$$

Q_{A} and M_{A} are the shear force and bending moment provided by the partial clamp at A. θ is the rotation angle of a small element of the strip at point (x, y). EI is the flexural rigidity of the elastic strip. s is the length of the

Table 1
Six elementary sub-domains

Case	Configuration
(a) Clamped–clamped	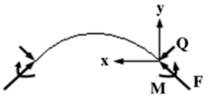
(b) Clamped–contact, outer wall	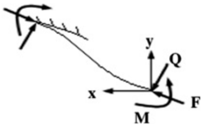
(c) Clamped–contact, inner wall	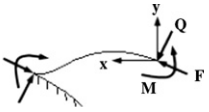
(d) Contact–contact, same wall	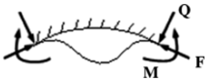
(e) Contact–contact, different walls	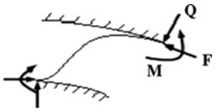
(f) Distributed contact	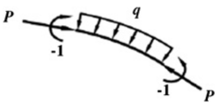

strip measured from point A. For convenience we introduce the following dimensionless parameters (with asterisks):

$$(s^*, x^*, y^*) = \frac{(s, x, y)}{r_{\mathrm{o}}}, \quad (Q_{\mathrm{A}}^*, F_{\mathrm{A}}^*) = \frac{r_{\mathrm{o}}^2}{\mathrm{EI}}(Q_{\mathrm{A}}, F_{\mathrm{A}}), \quad M_{\mathrm{A}}^* = \frac{r_{\mathrm{o}}}{\mathrm{EI}} M_{\mathrm{A}} \tag{2}$$

Eq. (2) represent the non-dimensionalization schemes for all lengths, forces, and moments in this paper. The dimensionless radii of the outer and inner walls are $r^* = 1$ and $r^* = \eta = \frac{r_{\mathrm{i}}}{r_{\mathrm{o}}}$, respectively. Similarly, we may introduce the dimensionless distributed force (per unit length) q^*, which will be used later, as

$$q^* = \frac{r_{\mathrm{o}}^3}{\mathrm{EI}} q \tag{3}$$

After substituting relations Eq. (2) into Eq. (1), and dropping all the superposed asterisks thereafter for simplicity, we obtain the dimensionless equilibrium equation

$$\frac{\mathrm{d}\theta}{\mathrm{d}s} = \left(-Q_{\mathrm{A}} \sin\frac{\psi}{2} - F_{\mathrm{A}} \cos\frac{\psi}{2}\right) y + \left(-Q_{\mathrm{A}} \cos\frac{\psi}{2} + F_{\mathrm{A}} \sin\frac{\psi}{2}\right) x + M_{\mathrm{A}} \tag{4}$$

After differentiating Eq. (4) with respect to s and noting the relations $\frac{\mathrm{d}y}{\mathrm{d}s} = \sin\theta$ and $\frac{\mathrm{d}x}{\mathrm{d}s} = \cos\theta$, we obtain

$$\frac{\mathrm{d}^2\theta}{\mathrm{d}s^2} = \left(-Q_{\mathrm{A}} \sin\frac{\psi}{2} - F_{\mathrm{A}} \cos\frac{\psi}{2}\right) \sin\theta + \left(-Q_{\mathrm{A}} \cos\frac{\psi}{2} + F_{\mathrm{A}} \sin\frac{\psi}{2}\right) \cos\theta \tag{5}$$

We multiply Eq. (5) by $\mathrm{d}\theta$ and integrate to obtain

$$\frac{1}{2}\left(\frac{\mathrm{d}\theta}{\mathrm{d}s}\right)^2 = Q_{\mathrm{A}} \sin\left(\frac{\psi}{2} - \theta\right) + F_{\mathrm{A}} \cos\left(\frac{\psi}{2} - \theta\right) + D_{\mathrm{A}} \tag{6}$$

D_{A} is an integration constant. From Eq. (6) we can write

$$\mathrm{d}s = \frac{\pm \mathrm{d}\theta}{U_{\mathrm{A}}} \tag{7}$$

where, U_{A} is defined as

$$U_{\mathrm{A}} = \sqrt{2Q_{\mathrm{A}} \sin\left(\frac{\psi}{2} - \theta\right) + 2F_{\mathrm{A}} \cos\left(\frac{\psi}{2} - \theta\right) + 2D_{\mathrm{A}}} \tag{8}$$

From Eq. (7) we obtain

$$\mathrm{d}x = \frac{\pm \cos\theta \, \mathrm{d}\theta}{U_{\mathrm{A}}} \tag{9}$$

$$\mathrm{d}y = \frac{\pm \sin\theta \, \mathrm{d}\theta}{U_{\mathrm{A}}} \tag{10}$$

The choice of "±" sign in Eqs. (7), (9), and (10) depends on the curvature of the deflection curve. If the curvature is positive, then "+" sign should be chosen, and vice versa. It is noted that $M_{\mathrm{A}} = \left(\frac{\mathrm{d}\theta}{\mathrm{d}s}\right)_{\theta = \frac{\psi}{2}}$. Therefore, we can calculate from Eq. (6) that

$$M_{\mathrm{A}} = \pm\sqrt{2F_{\mathrm{A}} + 2D_{\mathrm{A}}} \tag{11}$$

Whether M_{A} is positive or negative depends on the curvature at point A. Since the shear force at the middle point is zero, we have

$$Q_{\mathrm{A}} = F_{\mathrm{A}} \tan\frac{\psi}{2} \tag{12}$$

In most of the cases the deflection curve shows an inflection point N_1, at which the rotation angle is defined as θ_{N_1}. The curvature at the inflection point N_1 is zero. Therefore, D_{A} can be written from Eq. (6) as

$$D_{\mathrm{A}} = -Q_{\mathrm{A}} \sin\left(\frac{\psi}{2} - \theta_{N_1}\right) - F_{\mathrm{A}} \cos\left(\frac{\psi}{2} - \theta_{N_1}\right) \tag{13}$$

For this case Eqs. (6) and (8) can be written as

$$\frac{1}{2}\left(\frac{\mathrm{d}\theta}{\mathrm{d}s}\right)^2 = Q_{\mathrm{A}}\left[\sin\left(\frac{\psi}{2} - \theta\right) - \sin\left(\frac{\psi}{2} - \theta_{N_1}\right)\right] + F_{\mathrm{A}}\left[\cos\left(\frac{\psi}{2} - \theta\right) - \cos\left(\frac{\psi}{2} - \theta_{N_1}\right)\right] \tag{14}$$

$$U_{\mathrm{A}} = \sqrt{2\left(Q_{\mathrm{A}}\left[\sin\left(\frac{\psi}{2} - \theta\right) - \sin\left(\frac{\psi}{2} - \theta_{N_1}\right)\right] + F_{\mathrm{A}}\left[\cos\left(\frac{\psi}{2} - \theta\right) - \cos\left(\frac{\psi}{2} - \theta_{N_1}\right)\right]\right)} \tag{15}$$

After integrating Eq. (9) from $\theta = \frac{\psi}{2}$ to 0, we obtain the x-coordinate of the middle point C of the elastica as

$$x_{\mathrm{C}} = \left(\frac{1+\eta}{2}\right) \sin\frac{\psi}{2} = \int_{\frac{\psi}{2}}^{\theta_{N_1}} \frac{\cos\theta\,\mathrm{d}\theta}{U_{\mathrm{A}}} - \int_{\theta_{N_1}}^{0} \frac{\cos\theta\,\mathrm{d}\theta}{U_{\mathrm{A}}} \tag{16}$$

Similarly, the y-coordinate of point C can be calculated from Eq. (10) as

$$y_{\mathrm{C}} = \frac{1+\eta}{2} - \left(\frac{1+\eta}{2}\right) \cos\frac{\psi}{2} + \varepsilon = \int_{\frac{\psi}{2}}^{\theta_{N_1}} \frac{\sin\theta\,\mathrm{d}\theta}{U_{\mathrm{A}}} - \int_{\theta_{N_1}}^{0} \frac{\sin\theta\,\mathrm{d}\theta}{U_{\mathrm{A}}} \tag{17}$$

ε is the middle-point elevation of the strip measured upward from the median radius $(1+\eta)/2$. When the pushing force is small, the deflection curve has no inflection point. In such a case the right hand sides of Eqs. (16) and (17) are simplified to single integrals from $\theta = \frac{\psi}{2}$ to 0.

For the problem at hand, geometric parameters η and ψ, as well as the external compression F_{A}, are specified. There are five unknowns to be solved in this problem; they are Q_{A}, M_{A}, D_{A}, θ_{N_1}, and ε. First of all, Q_{A} can be calculated from Eq. (12) directly. After substituting Q_{A} into Eq. (16) we can solve for θ_{N_1}. After obtaining Q_{A} and θ_{N_1}, Eq. (13) can be used to determine D_{A}. Finally, M_{A} and ε can be calculated separately from Eqs. (11) and (17).

The shape of the elastica can be obtained by calculating the (x, y) coordinates of the deformed strip as follows: We start at point A at which the rotation angle ϕ of the deflection curve is $\frac{\psi}{2}$. Before the rotation angle reaches θ_{N_1} we use the formulas,

$$x = \int_{\frac{\psi}{2}}^{\phi} \frac{\cos\theta\,\mathrm{d}\theta}{U_{\mathrm{A}}}, \quad y = \int_{\frac{\psi}{2}}^{\phi} \frac{\sin\theta\,\mathrm{d}\theta}{U_{\mathrm{A}}} \tag{18}$$

After the rotation angle of the deflection curve passes θ_{N_1}, the formulas in Eq. (18) must be replaced by Eq. (19),

$$x = \int_{\frac{\psi}{2}}^{\theta_{N_1}} \frac{\cos\theta\,\mathrm{d}\theta}{U_{\mathrm{A}}} - \int_{\theta_{N_1}}^{\phi} \frac{\cos\theta\,\mathrm{d}\theta}{U_{\mathrm{A}}}, \quad y = \int_{\frac{\psi}{2}}^{\theta_{N_1}} \frac{\sin\theta\,\mathrm{d}\theta}{U_{\mathrm{A}}} - \int_{\theta_{N_1}}^{\phi} \frac{\sin\theta\,\mathrm{d}\theta}{U_{\mathrm{A}}} \tag{19}$$

After determining the shape, the dimensionless total length l of the elastica inside the channel from point A to B can be calculated as

$$l = \int \mathrm{d}s = 2\int_{\frac{\psi}{2}}^{\theta_{N_1}} \frac{\mathrm{d}\theta}{U_{\mathrm{A}}} - 2\int_{\theta_{N_1}}^{0} \frac{\mathrm{d}\theta}{U_{\mathrm{A}}} \tag{20}$$

The length Δl being pushed in the channel is $\Delta l = l - l_0$. The deformation pattern as described in this section and as observed in Fig. 3(1) is called deformation pattern 1 in this paper.

In this sub-section, we describe in detail the calculation procedure adopted in analyzing the elastica deformation. In other sub-domains as to be discussed later, we skip the detailed calculations and list only the main characteristics pertaining to the associated boundary conditions.

4.2. Clamped–contact sub-domains

Near the clamped end A, the elastica may contact the outer wall or the inner wall. Fig. 6 shows two possible scenarios; the elastica may contact the outer wall $r = 1$ at point H, or the elastica may contact the inner wall

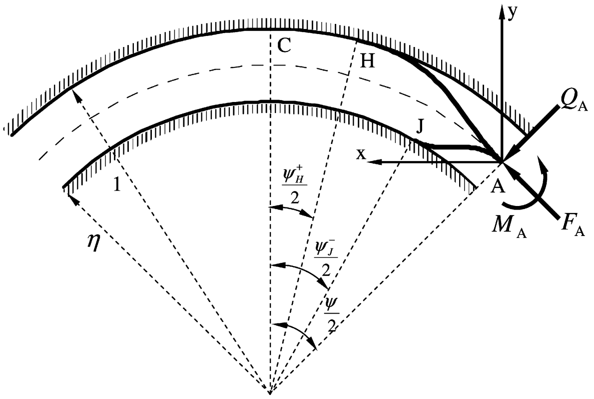

Fig. 6. Clamped–contact sub-domain.

$r = \eta$ at point J. The locations of point H and J may be denoted by the angles $\frac{\psi_H^+}{2}$ and $\frac{\psi_J^-}{2}$ as measured from the central radius, respectively. The superscripts "+" and "−" signify that the contact points are on the outer and inner walls, respectively. These two sub-domains are listed as cases (b) and (c) in Table 1.

In the case when the elastica is in point contact with the walls, the bending moments at points H and J are denoted as M_H and M_J, respectively. For point H we have

$$\left.\frac{d\theta}{ds}\right|_{\theta=\frac{\psi_H^+}{2}} = M_H \tag{21}$$

After substituting Eq. (21) into Eq. (6), we can obtain the following relation

$$\frac{M_H^2}{2} = Q_A \sin\left(\frac{\psi}{2} - \frac{\psi_H^+}{2}\right) + F_A \cos\left(\frac{\psi}{2} - \frac{\psi_H^+}{2}\right) + D_A \tag{22}$$

In the case when the contact becomes distributed, $M_H = -1$ and the integration constant D_A can be calculated as

$$D_A = \frac{1}{2} - Q_A \sin\left(\frac{\psi}{2} - \frac{\psi_H^+}{2}\right) - F_A \cos\left(\frac{\psi}{2} - \frac{\psi_H^+}{2}\right) \tag{23}$$

For point contact, Eq. (14) can also be modified to

$$\frac{M_H^2}{2} = Q_A\left[\sin\left(\frac{\psi}{2} - \frac{\psi_H^+}{2}\right) - \sin\left(\frac{\psi}{2} - \theta_{N_1}\right)\right] + F_A\left[\cos\left(\frac{\psi}{2} - \frac{\psi_H^+}{2}\right) - \cos\left(\frac{\psi}{2} - \theta_{N_1}\right)\right] \tag{24}$$

In the case when the contact becomes distributed, the shear force Q_A can be calculated as

$$Q_A = \frac{\frac{1}{2} - F_A\left[\cos\left(\frac{\psi}{2} - \frac{\psi_H^+}{2}\right) - \cos\left(\frac{\psi}{2} - \theta_{N_1}\right)\right]}{\left[\sin\left(\frac{\psi}{2} - \frac{\psi_H^+}{2}\right) - \sin\left(\frac{\psi}{2} - \theta_{N_1}\right)\right]} \tag{25}$$

If the contact occurs at point J on the inner wall, Eqs. (21) and (25) remain the same except that subscript "H" is replaced by "J," and the superscript "+" is replaced by "−." The equations formulated in this subsection can be used to determine the deflection curves involving clamped–contact sub-domain, such as in Fig. 3(2) and (3).

4.3. Contact–contact sub-domains

There are two types of contact–contact sub-domains. The first case is when both the contact points are on the outer wall, as shown by points H and I in Fig. 7(a). The second case is when the sub-domain contacts the

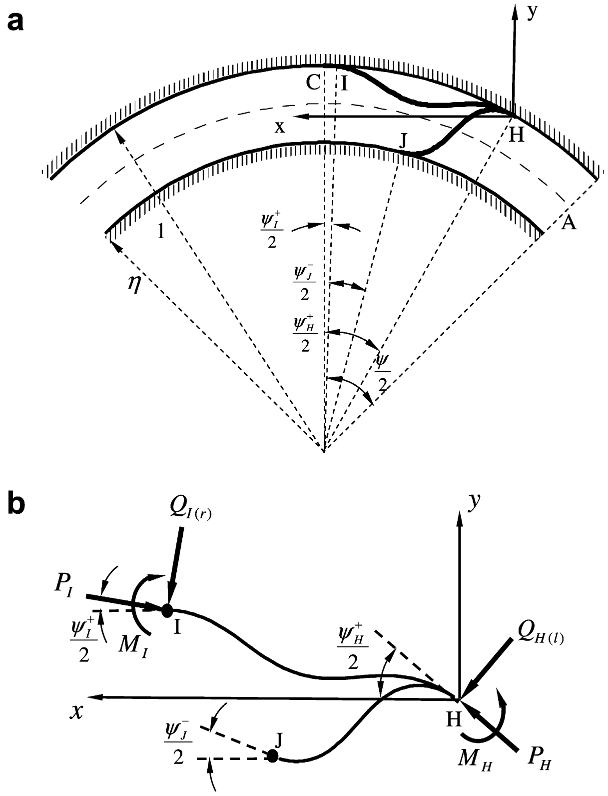

Fig. 7. (a) Contact–contact sub-domain. (b) Free body diagrams.

outer wall at one end and contacts the inner wall at the other end, as shown by points H and J in Fig. 7(a). The locations of points H, I, and J are signified by angles $\frac{\psi_H^+}{2}$, $\frac{\psi_I^+}{2}$, and $\frac{\psi_J^-}{2}$. These two scenarios are listed as cases (d) and (e) in Table 1. In our experiment, we never encounter the case when both the contact points are on the inner wall. Therefore, this scenario is omitted in this paper.

Fig. 7(b) shows the free body diagrams of these two sub-domains. We establish an *xy*-coordinate system with origin at point H. P_H, M_H, and $Q_{H(l)}$ are the longitudinal force, bending moment and shear force at point H. The subscript "*l*" in $Q_{H(l)}$ is to emphasize that the shear force is at a location slightly to the left of the contact point H. The rotation angle θ at H is equal to $\frac{\psi_H^+}{2}$. Following the same formulation as in Section 4.2, we can derive the equation

$$\frac{1}{2}\left(\frac{d\theta}{ds}\right)^2 = Q_{H(l)}\sin\left(\frac{\psi_H^+}{2}-\theta\right) + P_H\cos\left(\frac{\psi_H^+}{2}-\theta\right) + D_H \tag{26}$$

D_H is a new integration constant. From Eq. (26) we can write

$$ds = \frac{\pm d\theta}{U_H} \tag{27}$$

where,

$$U_H = \sqrt{2Q_{H(l)}\sin\left(\frac{\psi_H^+}{2}-\theta\right) + 2P_H\cos\left(\frac{\psi_H^+}{2}-\theta\right) + 2D_H} \tag{28}$$

After substituting the condition $\left.\frac{d\theta}{ds}\right|_{\theta=\frac{\psi_H^+}{2}} = M_H$ into Eq. (23) we have the relation

$$\frac{M_H^2}{2} = P_H + D_H \tag{29}$$

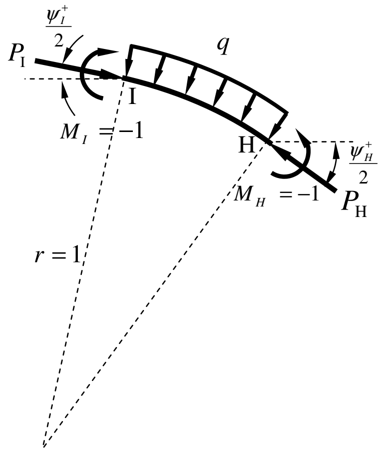

Fig. 8. Free body diagram in a distributed contact sub-domain.

In the special case when $M_{\mathrm{H}} = -1$ for distributed contact, D_{H} can be calculated as

$$D_{\mathrm{H}} = \frac{1}{2} - P_{\mathrm{H}} \tag{30}$$

The analysis for case (e) in Table 1 is similar. The equations formulated in this sub-section can be used to determine the deflection curves involving contact–contact sub-domain, such as in Fig. 3(4)–(12).

4.4. Distributed contact sub-domain

In some cases the elastica is in full contact with the outer radius over a finite segment, as listed in Table 1(f). We choose an arbitrary element HI from the fully contact segment and show the free-body diagram in Fig. 8. It can be shown that the distributed force q is a constant and is equal to P_{H}. First of all the moment balance equation about point I can be written as

$$\begin{aligned} -1 = & -1 + P_{\mathrm{H}} \sin\frac{\psi_{\mathrm{H}}^+}{2}\left(\sin\frac{\psi_{\mathrm{H}}^+}{2} - \sin\frac{\psi_{\mathrm{I}}^+}{2}\right) - P_{\mathrm{H}} \cos\frac{\psi_{\mathrm{H}}^+}{2}\left(\cos\frac{\psi_{\mathrm{I}}^+}{2} - \cos\frac{\psi_{\mathrm{H}}^+}{2}\right) \\ & - \int_{\frac{\psi_{\mathrm{I}}^+}{2}}^{\frac{\psi_{\mathrm{H}}^+}{2}} q\cos\theta\left(\sin\theta - \sin\frac{\psi_{\mathrm{I}}^+}{2}\right)\mathrm{d}\theta - \int_{\frac{\psi_{\mathrm{I}}^+}{2}}^{\frac{\psi_{\mathrm{H}}^+}{2}} q\sin\theta\left(\cos\frac{\psi_{\mathrm{I}}^+}{2} - \cos\theta\right)\mathrm{d}\theta \end{aligned} \tag{31}$$

After integration, Eq. (31) can be simplified to $q = P_{\mathrm{H}}$. This sub-domain can be found in some experimental observations, such as in Fig. 3(3), (5)–(6), and (8)–(12).

5. Deformation patterns

Each deformation described in the experimental observations in Section 3 can be divided into sub-domains as listed in Section 4 and solved theoretically. In the following, we first divide the deformation patterns into symmetric and asymmetric deformations. The calculations of some of these deformation patterns are straightforward, such as the deformation pattern 1 as explained in Section 4.1. Some of these deformation patterns are more complicated and require solving up to six coupled non-linear equations simultaneously. We refer the interested readers to the thesis of the first author for more details (Lu, 2007). In this paper we describe the features of these deformation patterns.

5.1. Symmetric deformation patterns

When the elastic strip is placed inside the circular channel and is under pushing force, the elastica deformation may be symmetric or asymmetric with respect to the central radius. In this section we first consider the symmetric deformation, which is more intuitive than the asymmetric one. In the following we divide the symmetric deformation patterns into four categories. Each category consists of several deformation patterns with similar characteristics. For symmetric deformations we only need to study one half of the elastica.

5.1.1. Deformation pattern 1–3

There are three deformation patterns in this category, as listed in Table 2. In the Table we also list the unknowns to be solved, the sub-domains involved, and the corresponding figure number of the experimental observation discussed in Section 3. Deformation pattern 1 is the first stage of the deformation and the detailed calculation has been discussed in Section 4.1. As external pushing force increases, the middle point will touch the outer wall, as shown in deformation pattern 2. The elastica is subject to a concentrated force at middle point C. As external force continues to increase, the point contact in the middle will become distributed contact over a finite region, as shown in deformation pattern 3. Beside the constant distributed force q over the contact region, the elastica is subject to an additional concentrated force R_{H}^{+} at point H. It is noted that the deflection curves presented in the Table are derived from numerical calculation with the pushing force F_{A} being specified as 3, 5, and 20, respectively.

5.1.2. Deformation pattern 4–7

Deformation pattern 3 as described above may branch into another series of deformation patterns in which the middle section of the elastica breaks away from the outer wall. These deformations are grouped in Table 3. In deformation pattern 4, the middle point of the elastica breaks away from the outer wall while the neighboring segments, such as segment IH, remain in distributed contact with the outer wall. The elastica is subject to a constant distributed force q. At the boundary of the contact region the elastica is subject to point forces R_{H}^{+} and R_{I}^{+}. The pushing force F_{A} needed to produce this deformation is 200. In deformation pattern 5 distributed contact segments reduce to point contact while the middle point of the elastica remains floating in the air. The pushing force F_{A} needed to produce this deformation is 100. With the same F_{A} the elastica may exhibit another deformation in which the middle point of the elastica

Table 2
Deformation pattern 1–3

	Deformation	Unknowns			Sub-domains	Exp. fig.
Pattern 1	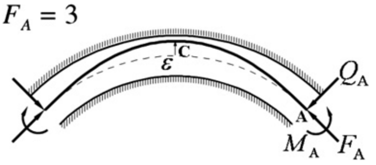	Q_{A} M_{A} D_{A}	θ_{N_1}	ε	(a)	3(1)
Pattern 2	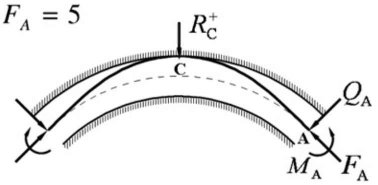	Q_{A} M_{A} D_{A}	θ_{N_1}	R_{C}^{+}	(b)	3(2)
Pattern 3	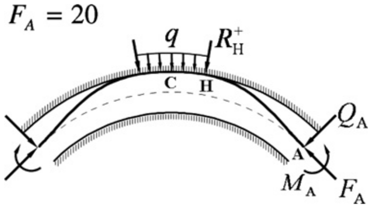	Q_{A} M_{A} D_{A}	θ_{N_1} ψ_{H}^{+}	R_{H}^{+} q	(b)(f)	3(3)

Table 3
Deformation pattern 4–7

	Deformation	Unknowns				Sub-domains	Exp. fig.
Pattern 4	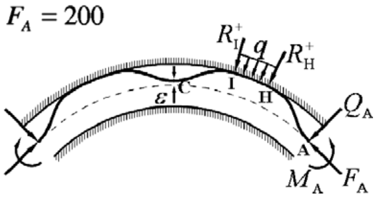	Q_A M_A D_A D_I	θ_{N_1} θ_{N_2} ψ_H^+ ψ_I^+	R_H^+ q R_I^+	ε	(b)(d)(f)	3(5)
Pattern 5	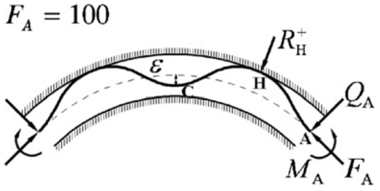	Q_A M_A D_A D_H	θ_{N_1} θ_{N_2} ψ_H^+	R_H^+	ε	(b)(d)	3(4)
Pattern 6	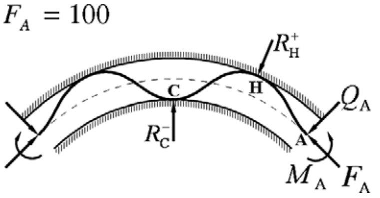	Q_A M_A D_A D_H	θ_{N_1} θ_{N_2} ψ_H^+	R_H^+ R_C^-		(b)(e)	3(7)
Pattern 7	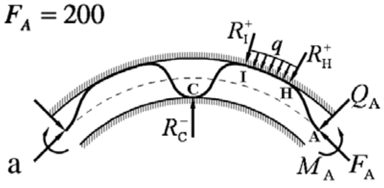	Q_A M_A D_A D_I	θ_{N_1} θ_{N_2} ψ_H^+ ψ_I^+	R_H^+ q R_I^+ R_C^-		(b)(e)(f)	3(8)
							3(12)

touches the inner wall while the neighboring segments remains point contact with the outer wall. This is deformation pattern 6. As F_A increases, the point contacts on the outer wall in deformation pattern 6 become distributed. This is denoted as deformation pattern 7. However, it is found that for the same $F_A = 200$, we can solve for two different but similar deformation configurations. We denote them as patterns 7a and 7b, which involve regular and Ω-shaped folding segments, respectively. It is clear from this Table that multiple equilibrium configurations are very common in constrained elastica. For instance, when $F_A = 200$ the elastica may exhibit deformation patterns 4, 7a, and 7b.

5.1.3. Deformation pattern 8–11

There are four deformation patterns in Table 4, which have three contacts on the outer wall. In deformation pattern 8 the elastica is in distributed contact with the outer wall in regions HI and KC. θ_{N_1} is the rotation angle of the inflection point in segment AH. θ_{N_2}, and θ_{N_3} are the two inflection points in segment IK. The pushing force producing the deflection curve plotted in the table is $F_A = 400$. It is noted that we are unable to produce this deformation pattern in our experiment. The two folding segments appear to have a tendency to snap back to the outer wall.

Table 4
Deformation pattern 8–11

	Deformation	Unknowns			Sub-domains	Exp. fig.
Pattern 8	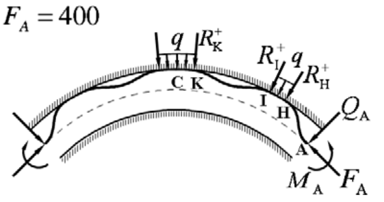	Q_A M_A D_A D_I	θ_{N_1} θ_{N_2} θ_{N_3} ψ_H^+ ψ_I^+ ψ_K^+	R_H^+ q R_I^+ R_K^+	(b)(d)(f)	None
Pattern 9	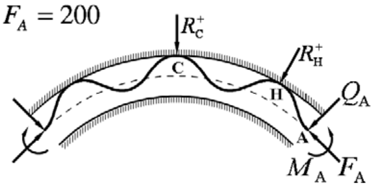	Q_A M_A D_A D_H	θ_{N_1} θ_{N_2} θ_{N_3} ψ_H^+	R_H^+ R_C^+	(b)(d)	4(1)
Pattern 10	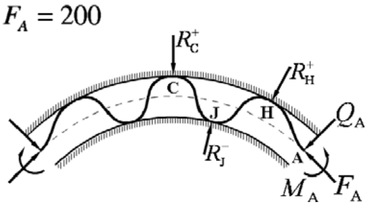	Q_A M_A D_A D_H D_J	θ_{N_1} θ_{N_2} θ_{N_3} ψ_H^+ ψ_J^-	R_H^+ R_J^- R_C^+	(b)(e)	4(2)
Pattern 11	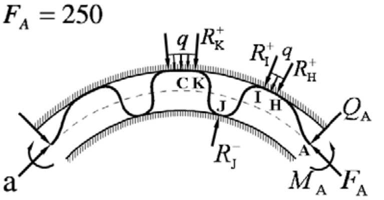 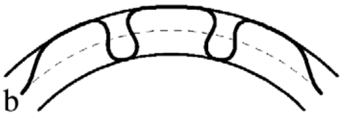	Q_A M_A D_A D_I D_J	θ_{N_1} θ_{N_2} θ_{N_3} ψ_H^+ ψ_I^+ ψ_J^- ψ_K^+	R_H^+ q R_I^+ R_J^- R_K^+ q_K	(b)(e)(f)	4(3) 4(10)

In deformation pattern 9 the distributed contacts on the outer wall are reduced to point contacts when F_A decreases to 200. With the same F_A, the elastica can be in deformation pattern 10, which is similar to deformation 9 except that the elastica is in point contact with the inner wall at point J. Deformation pattern 11 is similar to deformation pattern 10, except that the point contacts on the outer wall become distributed contacts. In the Table we show that for the same $F_\mathrm{A} = 250$, there exist two similar but slightly different configurations, denoted as 11a (regular folding segments) and 11b (Ω-shaped folding segments).

5.1.4. Deformation pattern 12

Deformation pattern 12, as listed in Table 5, is unique in the sense that the curvatures of the deflection curve near the clamped ends are negative. The elastica is in distributed contact with the outer wall in the middle segment, while it is in point contact with the inner wall near the ends. It is noted that for the same pushing force $F_\mathrm{A} = 200$ there exist two symmetric deformation patterns, denoted as 12a (regular) and 12b (Ω-shaped).

Table 5
Deformation pattern 12

	Deformation	Unknowns			Sub-domains	Exp. fig.
Pattern 12	$F_A = 200$ 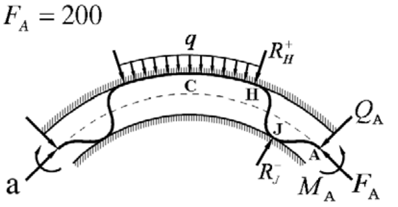	Q_A	θ_{N_1}	R_J^-		
		M_A	θ_{N_2}	R_H^+		
		D_A	ψ_J^-	q		5(2)
		D_J	ψ_H^+		(c)(e)	
						5(5)

5.2. Asymmetric deformation patterns

5.2.1. Deformation patterns 4′, 7′, 8′, and 11′

Asymmetric deformations may occur even if the boundary conditions at both ends of the elastica are symmetric. A special type of asymmetric deformation can be considered as a variation of some of the symmetric deformations discussed in Section 5.1. One common feature of these symmetric deformations is that they all possess more than two segments of distributed contact on the outer wall; for instance, deformation patterns 4, 7, 8, and 11. We use the superposed prime to distinguish these asymmetric deformations from their symmetric counterparts. Table 6 lists the deformation patterns 4′ and 7′. Table 7 lists

Table 6
Deformation patterns 4′ and 7′

	Deformation	Sub-domains	Exp. fig.
Pattern 4′	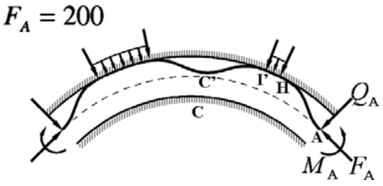	(b)(d)(f)	3(6)
Pattern 7′	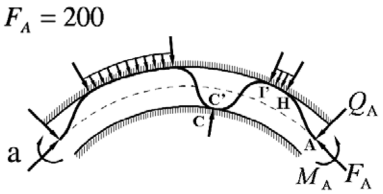	(b)(e)(f)	3(9)
			3(10)
	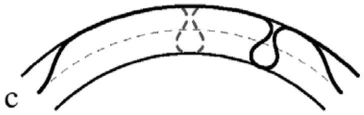		3(11)

Table 7
Deformation patterns 8′ and 11′

	Deformation	Sub-domains	Exp. fig.
Pattern 8′	$F_A = 400$ 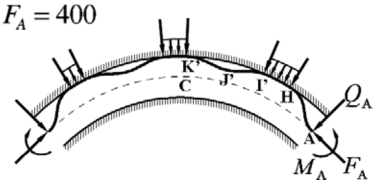 	(b)(d)(f)	None
Pattern 11′	$F_A = 250$ 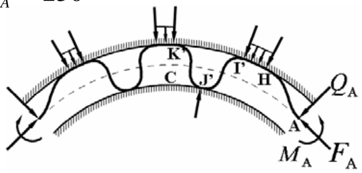 a	(b)(e)(f)	4(4)
	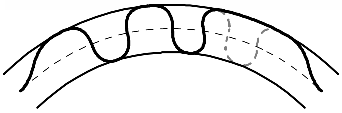 b		4(5)
	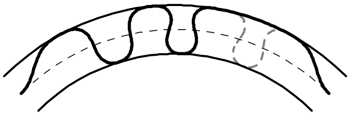 c		4(6)
	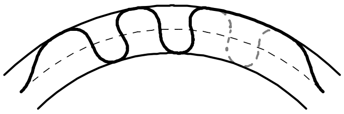 d		4(7)
	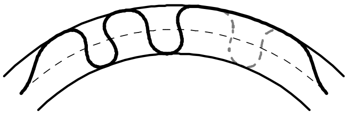 e		4(8)
	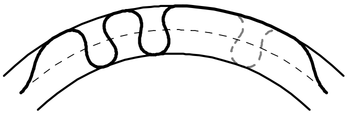 f		4(9)

the deformation patterns 8′ and 11′. Similar to deformation pattern 8, we are unable to produce deformation patterns 8′ in the experiment. Since the calculation methods involved in these asymmetric deformations are basically the same as those used in their symmetric counterparts, the unknowns to be solved are omitted in these Tables.

The reason why these asymmetric deformations coexist with their symmetric counterparts for exactly the same pushing force can be explained with a specific example, for instance, deformation patterns 4′ as shown in Fig. 9. It is noted that the location of the first contact point H from clamp A is determined once the pushing force F_A is specified. This statement is valid only when the contact near point H is distributed (Lu, 2007). However, the location of the point I, the other boundary point of the distributed contact region, can be determined only when the equilibrium and the geometric condition on segment CI is considered at the same time. In the calculation, if we specify that the point C of the middle folding segment lies on the central radius, we will obtain the symmetric deformation 4 as before. However, if we relax this symmetric condition and allow the middle point of the folding segment to be away from the central radius, such as at position C' in Fig. 9, then the equilibrium condition as well as this new geometric condition can still be satisfied with a different location

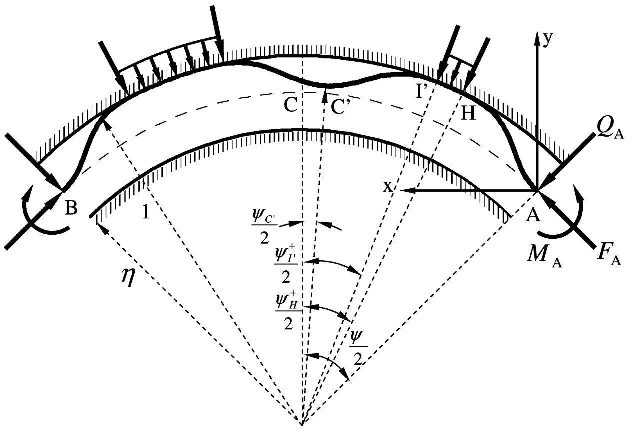

Fig. 9. Deformation pattern 4′.

of point I, denoted now as I′. As to the left half of the elastica, since the pushing force on the left end is the same as the one on the right end, the location of the first contact point from the left will be symmetric with respect to the one on the right. However, the contact region on the left will be of different size. As a consequence, the elastica deformation exhibits asymmetric pattern 4′. The location of the middle point C of the folding segment can be in any place within the range $0 < \frac{1}{2}\psi_{C'} < \frac{1}{2}(\psi_H^+ - \psi_I^+)$, where $\frac{\psi_H^+}{2}$ and $\frac{\psi_I^+}{2}$ are angles of point H and I in symmetric deformation pattern 4. In other words, in the solution procedure, if we specify $\psi_{C'} = 0$, we will obtain deformation pattern 4. On the other hand, if we specify a non-zero $\psi_{C'}$ within the range, we will obtain asymmetric deformation pattern 4′ with the same equations. The pushing force F_A producing the deflection curve in Fig. 9 is 200.

The same argument applies to the calculations of variations 7′, 8′ and, 11′, with more complexities. Table 6 shows three different types of asymmetric deformation 7′ for the pushing force $F_A = 200$. Deformation patterns 7′a and 7′c are the variations of 7a and 7b in Table 3. Besides these two variations there is one additional asymmetric deformation 7′b, which has a slanted folding segment. The dashed curves in 7′b and 7′c show the left extreme position of the folding segments, while the solid curves represent the right extreme positions of the folding segment. The folding segments of the asymmetric equilibrium configuration can be in any place within the range of the dashed and solid curves.

Similar situations occur for asymmetric deformations 8′ and 11′, as shown in Table 7. The relations between the six variations of 11′ can be explained as follows. The left folding segments of 11′a, 11′b, and 11′c are of the regular type. However, the right folding segments may be regular (11′a), slanted (11′b), and Ω-shaped (11′c). The last three deformations are the other possible combinations of the folding segments, i.e., slanted–slanted (11′d), Ω-shaped–slanted (11′e), and Ω-shape-Ω-shaped (11′f). All these six variations can be observed in the experiment. Again the dashed curves represent the right extreme positions of the right folding segments of these asymmetric equilibrium configurations when the left folding segments are fixed to the extreme left positions. Similarly, the left folding segments can be moved freely within certain ranges which are not shown in the Table.

It is noted that deformations 11′a and 11′f are the asymmetric variations of 11a and 11b, respectively. If the left folding segments of these two configurations are moved in the same manner as their right counterparts but in the opposite direction, the resulted variation will be again symmetric with respect to the central radius. Therefore, the symmetric deformations 11a and 11b in Table 4 can have infinite number of symmetric variations. Similarly, deformation 8 in Table 4 can also have infinite number of symmetric variations by moving the right and left folding segments symmetrically.

5.2.2. Deformation pattern 12′

The symmetric deformation 12 as listed in Table 5 also has asymmetric variation. It is noted that deformation 12 has only one segment of distributed contact on the outer wall. For $F_A = 200$, there exist two different symmetric deformations configurations 12a and 12b. The asymmetric variation 12′ involves the combination of these two symmetric configurations, as shown in Table 8.

5.2.3. Deformation pattern 3 + 12

The asymmetric deformations 4′, 7′, 8′, 11′, and 12′ discussed above have identical pushing forces on both ends. Another kind of asymmetric deformation involving the combination of deformation patterns 3 and 12, denoted as 3 + 12 in this paper. For this type of asymmetric deformation the pushing forces on the two ends are different. The common feature of deformation patterns 3 and 12 is that they both have a distributed contact segment in the middle. If we start with deformation pattern 3 on the left, the location of the boundary point I of the distributed contact region depends only on the pushing force F_B on the left end. This deformation pattern 3 on the left may coexist with a deformation pattern 12 on the right with an opposite curvature near the end A. Again, the deformation on the right depends only on the pushing force F_A. However, the common contact segment in the middle requires that the longitudinal forces at point H and I be identical. This condition gives us the relation between F_A and F_B. Since there exist two different deformation patterns 12 for the same pushing force F_A, there exist two different combinations in Table 9, denoted as 3 + 12a and 3 + 12b, respectively.

5.2.4. Deformation pattern 11 + 12

Another kind of asymmetric deformation involves the combination of deformation patterns 11 and 12, as shown in Table 10. For the same pushing force, there exist three different deformations 11 and two different deformations 12. Therefore, there are six combinations of 11 + 12 as listed in Table 10. All of these six deformation patterns can be realized in the experiment as discussed in Fig. 5.

Table 8
Deformation pattern 12′

	Deformation	Sub-domains	Exp. fig.
Pattern 12′	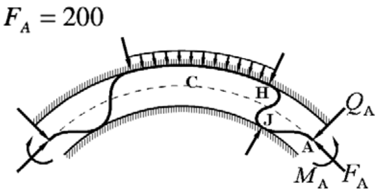	(b)(d)(f)	5(4)

Table 9
Deformation pattern 3 + 12

	Deformation	Unknowns				Sub-domains	Exp. fig.
Pattern 3 + 12	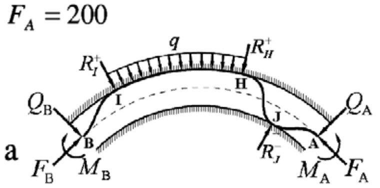	Q_A M_A D_A D_J D_I	θ_{N_1} θ_{N_2} θ_{N_3} ψ_J^- ψ_H^+ ψ_I^+	R_J^- R_H^+ q R_I^+	F_B Q_B M_B	(b)(c)(e)(f)	5(1)
							5(3)

Table 10
Deformation pattern 11 + 12

	Deformation	Unknowns				Sub-domains	Exp. fig.
Pattern 11 + 12	$F_A = 200$ a 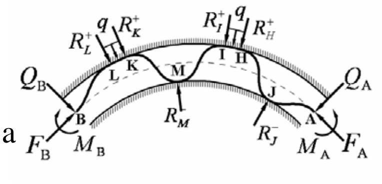	Q_A M_A D_A D_J D_I D_M D_L	θ_{N_1} θ_{N_2} θ_{N_3} θ_{N_4} θ_{N_5} ψ_J^- ψ_H^+ ψ_I^+ ψ_M^- ψ_K^+ ψ_L^+	R_J^- R_H^+ q R_I^+ R_M^- q_K R_L^+	F_B Q_B M_B	(b)(c)(e)(f)	5(6)
	b 						5(7)
	c 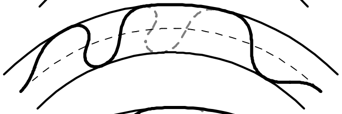						5(8)
	d 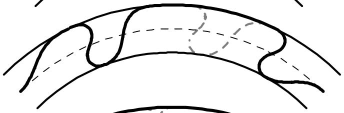						5(9)
	e 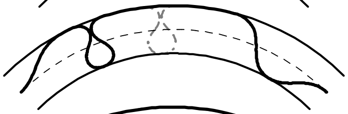						5(10)
	f 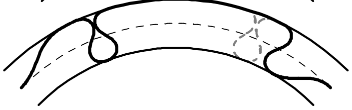						5(11)

6. Load-deflection relations

6.1. Theoretical predictions

In this sub-section we present the theoretical relation between the longitudinal forces at both ends (F_A and F_B) and the elastica length increment Δl inside the channel. In Figs. 10 and 11, the longitudinal force F_B at the left end is equal to the external pushing force F_A. In Fig. 12, however, F_B will be in general different from F_A, and we show only the relation between F_B and Δl. These predictions will be compared to experimental measurements in the next sub-section.

In Fig. 10 we first show the loading procedure starting from pattern 1–3, in which F_A increases almost exponentially as Δl increases. On the load-deflection curves we use black dots to signify the boundary of various deformation patterns. The load-deflection curve corresponding to deformation patterns 1–2–3 can go beyond the range of the figure. However, we observe another branch of load-deflection curve corresponding to deformation patterns 4, 4′–5–6–7a, 7′a. At $\Delta l = 0.46$, the load-deflection curve branches into two curves corresponding to deformation patterns 7′b and 7b, 7′c, respectively. It is noted that the deformation patterns 4 and 4′ coexist for the same F_A and Δl, so do 7a and 7′a, and 7b and 7′c. It is noted that curve 1–2–3 does not intersect curve 4, 4′–5–6–7a, 7′a. Therefore, there will be no buckling from deformation 3–4. This is unlike the case with straight channel in which the load-deflection curves are continuous (Domokos et al., 1997). For fixed Δl, say, 0.16, there may coexist four deformation patterns, i.e., 3, 4, 4′, and 5. In order for the elastica deformation to jump from 3 to 4, for instance, pulling and pushing action on the interior of the elastica by

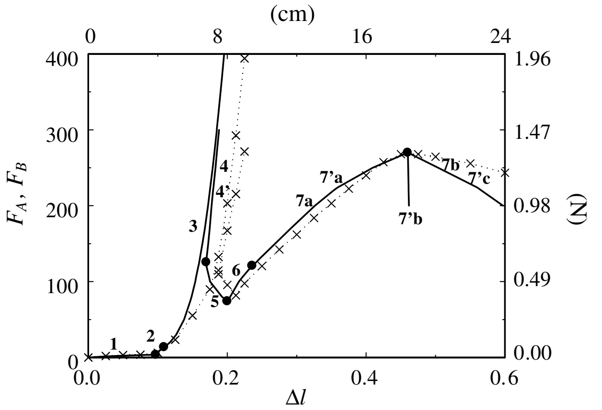

Fig. 10. Load-deflection curves for patterns 1–3 and 4–7. Cross mark × represents the relation between the measured longitudinal force F_B and Δl.

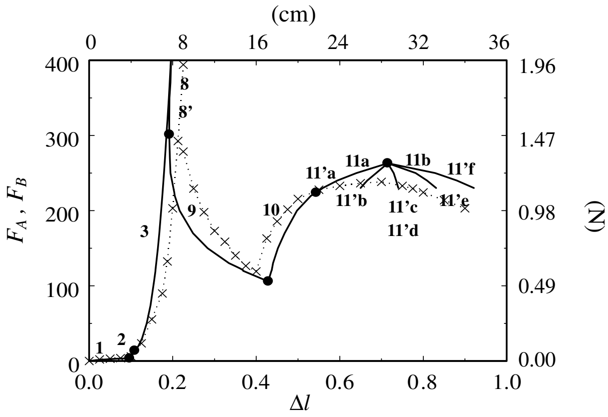

Fig. 11. Load-deflection curves for patterns 1–3 and 8–11. Cross mark × represents the relation between the measured longitudinal force F_B and Δl.

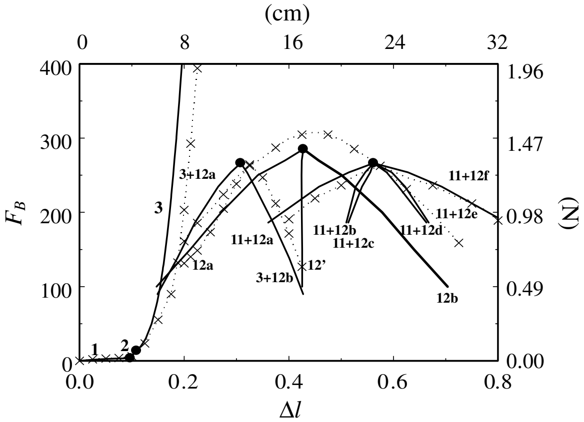

Fig. 12. Load-deflection curves for patterns 1–3 and 12, 12′, 3 + 12, 11 + 12. Cross mark × represents the relation between the measured longitudinal force F_B and Δl.

hand is needed in the experiment. On the other hand, if we fix the pushing force F_A, say at 200, there may coexist 8 deformation patterns, i.e., 3, 4, 4′, 7a, 7b, 7′a, 7′b, and 7′c.

In Fig. 11 we show the load-deflection curve corresponding to deformations 8, 8′–9–10. Although this curve is very close to the curve 1–2–3, they do not intersect either. The load-deflection curve corresponding to deformation 10 evolves to patterns 11a and 11′a, which is one of the five branches merging at $\Delta l = 0.71$. The other four branches are 11′b, 11′c and 11′d, 11′e, and 11b and 11′f. It is emphasized that deformation 11a coexists with 11′a, 11′c coexists with 11′d, and 11b coexists with 11′f. The branching behavior of the load-deflection curve in Fig. 11 is similar to the one observed in Fig. 10. The main difference between Figs. 10 and 11 is that deformations in Fig. 10 have one folding segment, while the deformations in Fig. 11 have two folding segments.

Fig. 12 shows more load-deflection curves corresponding to other asymmetric deformations. Beside the deformations 1–2–3, there are three families of deformations in Fig. 12. The first family consists of two branches corresponding to deformations 3 + 12a and 3 + 12b. The second family to the right consists of 3 branches corresponding to deformations 12a, 12′, and 12b. The third family consists of six branches corresponding to the six deformations 11 + 12a, 11 + 12b, 11 + 12c, 11 + 12d, 11 + 12e, and 11 + 12f. It is emphasized that the longitudinal forces F_B in these deformation patterns are different from the external pushing forces F_A. The relation between F_A and Δl is very similar to the one in Fig. 12, with only slight difference (almost indistinguishable) in force magnitudes (Lu, 2007).

6.2. Experimental measurements

In order to verify the theoretical predictions presented in the previous sub-section, we measured the longitudinal reactive force F_B at the left end with a load cell. The measured relations between F_B and Δl are plotted with cross mark × in Figs. 10–12. The cross marks are connected by dotted lines in order to compare with the theoretical predictions. For convenient reference, we present the measured results with both dimensionless parameters (left and bottom sides) and the physical ones (right and top sides).

We first examine the experimental data in Fig. 10. For the deformation pattern 1–3 in Fig. 10 (also in Figs. 11 and 12), the measured F_B are generally smaller than the theoretical predictions. This is mainly due to the friction effect in the contact region. This is especially true in deformation pattern 3, which involves extensive distributed contact. In this paper we do not consider friction in the theoretical formulation.

The range of Δl (approximately from 8 to 9.5 cm) for deformation pattern 4 in Fig. 10 is small. In addition, this deformation pattern also involves distributed contact like deformation pattern 3. As a consequence the measured F_B in deformation pattern 4 are also smaller than the theoretical prediction. Deformation patterns 5 and 6 in Fig. 10 involve only point contact. As a consequence, the friction effect is less significant and the agreement between experiment and theory improves. The agreement between theory and experiment in deformation pattern 7a is surprisingly good. However, the agreement in deformation pattern 7b deteriorates again. The range of Δl for deformation pattern 7′b is too small, which prevents us from making reliable force measurement.

In Fig. 11 we are unable to produce deformation pattern 8. In both deformation patterns 9 and 10, the measured F_B are generally larger than theory. However, when the deformation evolves to pattern 11 (branches a and b), the measured F_B become smaller than the theoretical ones. The measurements on the other three branches of deformation pattern 11 are not recorded because reliable force readings are difficult to obtain due to the large friction force involved in the experiment.

In Fig. 12 the agreement between theory and experiment in deformation patterns 3 + 12 (branches a and b) and 11 + 12 (branches a and f) are generally satisfactory. However, in deformation pattern 12 (branches a and b) the measured F_B are significantly larger than the theoretical ones. Generally speaking, in spite of the measurement error, the general trends of the theoretical and experimental load-deflection curves agree fairly well in Figs. 10–12.

7. Discussions and conclusions

In this paper, we study the planar deformations of an elastica inside a circular channel with clearance. One end of the elastica is fully clamped, while the other end is partially clamped in the lateral direction and is subject to a pushing force in the longitudinal direction. Theoretical prediction of the deformation patterns are compared with experimental results both qualitatively and quantitatively. Several discussions and conclusions can be summarized as follows.

(1) Both symmetric and asymmetric deformations are possible theoretically and observable in the laboratory although the boundary conditions are always symmetric. This is also the case in the experiment of Domokos et al. (1997) with straight channel. This is probably because displacement control is adopted in both experiments. Whether asymmetric deformation is still possible in a load control experiment remains a topic of future research. In order to answer this question, a rigorous study on the stability of constrained elastica is needed.
(2) If one end of the elastica is pushed into the channel quasi-statically, no buckling will occur. In order for the elastica to jump from deformation 3 (elastica pushed against the wall) to 4 (elastica off the wall), pulling the interior of the elastica is required. In the case of a straight channel, on the other hand, deformation 3 will bifurcate to deformation 4 automatically when the elastica is pushed in. This phenomenon is a symmetrical pitchfork bifurcation with the branch corresponding to deformation 3 being cut off by another branch corresponding to deformation 4 due to the straight wall. In circular channel the curvature of the wall appears as an imperfection and the pitchfork disintegrates into a continuous branch (elastica pushed against the wall) and a disconnected branch (elastica off the wall).
(3) We observe that in the case when the deformation patterns involve point contacts on the outer wall, the equilibrium configurations are isolated. On the other hand, if the deformation patterns involve distributed contacts on the outer wall, it is possible to move the folding segments freely within certain range. This phenomenon permits the existence of the asymmetric variation of a symmetric deformation. Holmes et al. (1999) also reported similar results in their experiment with straight channel.

References

Chai, H., 2002. On the post-buckling behavior of bilaterally constrained plates. International Journal of Solids and Structures 39, 2911–2926.

Chai, H., 2006. On the crush worthiness of a laterally confined bar under axial compression. Journal of Applied Mechanics 73, 834–841.

Chen, J.-S., Li, C.W., 2007. Planar elastica inside a curved tube with clearance. International Journal of Solids and Structures 44, 6173–6186.

Cunha, J.C., 2004. Buckling of tubulars inside wellbores: review on recent theoretical and experimental works. SPE Drilling and Completion 19, 13–19.

Domokos, G., Holmes, P., Royce, B., 1997. Constrained Euler buckling. Journal of Nonlinear Science 7, 281–314.

Holmes, P., Domokos, G., Schmitt, J., Szeberenyi, I., 1999. Constrained Euler buckling: an interplay of computation and analysis. Computer Methods in Applied Mechanics and Engineering 170, 175–207.

Huang, N.C., Pattillo, P.D., 2000. Helical buckling of a tube in an inclined wellbore. International Journal of Non-Linear Mechanics 35, 911–923.

Kuru, E., Martinez, A., Miska, S., Qiu, W., 2000. The buckling behavior of pipes and its influence on the axial force transfer in directional wells. Journal of Energy Resources Technology 122, 129–135.

Love, A.E., 1944. A Treatise on the Mathematical Theory of Elasticity. Dover Publications, New York.

Lu, Z.-H., 2007. Deformations of a Planar Elastica inside a Circular Channel with Clearance, MS Thesis, Department of Mechanical Engineering, National Taiwan University.

Paslay, P.R., Bogy, D.B., 1964. The stability of a circular rod laterally constrained to be in contact with an inclined circular cylinder. Journal of Applied Mechanics 31, 605–610.

Plaut, R.H., Suherman, S., Dillard, D.A., Williams, B.E., Watson, L.T., 1999. Deflections and buckling of a bent elastica in contact with a flat surface. International Journal of Solids and Structures 36, 1209–1229.

Plaut, R.H., Taylor, R.P., Dillard, D.A., 2004. Postbuckling and vibration of a flexible strip clamped at its ends to a hinged substrate. International Journal of Solids and Structures 41, 859–870.

Pocheau, A., Roman, B., 2004. Uniqueness of solutions for constrained elastica. Physica D 192, 161–186.

Roman, B., Pocheau, A., 2002. Postbuckling of bilaterally constrained rectangular thin plates. Journal of the Mechanics and Physics of Solids 50, 2379–2401.

Timoshenko, S.P., Gere, J.M., 1961. Theory of Elastic Stability. McGraw Hill, New York.

Wu, J., Juvkam-Wold, H.C., 1995. The effect of wellbore curvature on tubular buckling and lockup. Journal of Energy Resources Technology 117, 214–218.